In situ self-assembled synthesis of Ag-AgBr/Al-MCM-41 with excellent activities of adsorption-photocatalysis

Yuan Guan [a,b], Shaomang Wang [a,c,*], Xin Wang [b,**], Cheng Sun [d], Yan Huang [a], Cheng Liu [a], Hongyun Zhao [a]

[a] School of Petrochemical Engineering, School of Environment and Safety Engineering, School of Huai De, Changzhou University, Changzhou 213164, China
[b] Key Laboratory for Soft Chemistry and Functional Materials of Ministry Education, Nanjing University of Science and Technology, Nanjing 210094, China
[c] Eco-Materials and Renewable Energy Research Center (ERERC), College of Engineering and Applied Sciences, Nanjing University, Nanjing 210093, China
[d] State Key Laboratory of Pollution Control and Resource Reuse, School of the Environment, Nanjing University, Nanjing 210023, China

ABSTRACT

A novel material of Ag-AgBr/Al-MCM-41 with dual functions of adsorption-photocatalysis was synthesized by installing Ag-AgBr on the Al-MCM-41 from natural palygorskite using in situ self-assembled method. The activities of adsorption-photocatalysis of 50% Ag-AgBr/Al-MCM-41 were significantly higher than those of Ag-AgBr, 50% Ag-AgBr/Pal and 50% Ag-AgBr/MCM-41. After adsorption for 30 min and light irradiation for 210 min, the removal rate of 100 mL of 50 mg L^{-1} basic fuchsin (crystal violet, aniline) over 50% Ag-AgBr/Al-MCM-41 (50 mg) was about 98% (99%, 90%). The Al-MCM-41 from natural palygorskite not only provided large specific surface area, but also uniformly anchored Ag-AgBr due to the in situ self-assembled approach. This greatly enhanced performances of adsorption-photocatalysis of 50% Ag-AgBr/Al-MCM-41. In addition, SPR effect of Ag broadened light absorption range of 50% Ag-AgBr/Al-MCM-41 and favored separation of carriers, which drastically improved its photocatalytic activity.

© 2017 Published by Elsevier B.V.

1. Introduction

Efficient and low-cost treatment of hazardous organic pollutants in water has been a hot topic of widespread concern [1–5]. Since TiO$_2$ was found to be able to split water under ultraviolet (UV) light, semiconductor photocatalysis has been widely recognized as a promising technology for the treatment of toxic organic contaminants in water [6–13]. However, the lack of high-performance photocatalysts has limited the practical application of this technology. Great efforts have been made to fabricate photocatalysts with high photocatalytic activity.

Noble metal nanoparticles (NPs) as co-catalysts have attracted much attention owing to the effect of surface plasmon resonance (SPR), which can drastically improve photocatalytic performance of a photocatalyst. In recent years, many photocatalysts based on surface plasmon resonance such as Ag/SBA-15 [14,15], Pa-Ag/SBA [16,17], Ag@C$_3$N$_4$ [18], CQDs/Ag/Ag$_3$PO$_4$ [19], Au/CeO$_2$ [20] and Au/TiO$_2$ [21,22] have been developed and exhibited excellent photocatalytic activities. Since Huang et al. first synthesized a plasmonic photocatalyst of Ag–AgCl [23], silver/silver halides with surface plasmon resonance such as AgCl/Ag [24], Ag@Ag(Cl,Br) and Ag@AgCl-AgI [25], Ag/AgBr [26–30] and Ag/AgI [31,32] have been intensively investigated due to their excellent photocatalytic activities. Among them, Ag-AgBr with appropriate energy of band-gap and potentials of conduction-band edge and valence-band edge obtains the most attention. However, Ag-AgBr is still difficult to efficiently degrade toxic organic contaminants with heavy concentrations in water.

Loading silver bromide on the carriers is an effective method to improve its capability for the removal of highly concentrated pollutants by adsorption- photocatalysis. Many carriers such as activated carbon [33], graphene-oxide [34], carbon nanotubes [35], palygorskite [36] and γ-Al$_2$O$_3$ [37] were used to load Ag-AgBr. However, a common method of depositing Ag-AgBr on a carrier easily results in the aggregation of active particles on the surface of the carrier, which generally destroys channel structure of the carrier, thereby reducing performances of adsorption-photocatalysis of this composite.

The aim of this work is to prepare a novel material of Ag-AgBr/Al-MCM-41 with excellent activities of adsorption-photocatalysis by

---

* Corresponding author at: Key Laboratory for Soft Chemistry and Functional Materials of Ministry Education, Nanjing University of Science and Technology, Nanjing, 210094, China.
** Corresponding author.
E-mail addresses: gywsm@cczu.edu.cn (S. Wang), wangx@njust.edu.cn (X. Wang).

loading Ag-AgBr on the Al-MCM-41 from natural palygorskite using in situ self-assembled method. The performances of adsorption-photocatalysis of Ag-AgBr/Al-MCM-41 with different content of Ag-AgBr will be evaluated by comparing removal rates of basic fuchsin (BF), crystal violet (CV) and aniline from water, respectively. The enhanced activities of adsorption-photocatalysis of Ag-AgBr/Al-MCM-41 and the removal mechanisms of organic contaminants will be discussed in detail.

2. Experimental section

2.1. Materials

Palygorskite (Pal, effective substance >99 wt%) with an average diameter of 74 μm was provided by Jiangsu Pal Co. Ltd (china). Hydrochloric acid (HCl, 37%), nitric acid (HNO₃, 69%), sodium hydroxide (NaOH), cetyltrimethyl ammonium bromide (CTAB), polyethylene glycol 4000 (PEG) and silver nitrate (AgNO₃) were purchased from sinopharm chemical reagent Co. Ltd (China).

2.2. Preparation of Ag-AgBr/Al-MCM-41

20 g of Pal was treated by 80 mL of HCl (6 mol L^{-1}) for 3 h at 60 °C. It was filtered, washed with deionized water to pH value of 7 and then dried at 80 °C for 12 h. HCl-acidified Pal was achieved and stored in a desiccator for further use.

10 g of acidified Pal and 15 g of NaOH were ball-milled together and calcined in air at 550 °C for 5 h. The mixture was added into 100 mL of deionized water and stirred vigorously for 12 h to obtain the suspension. Then the extracted solution containing silica aluminum source was separated from the suspension by a filtration process.

An equal amount of CTAB and PEG was dissolved into 30 mL of deionized water. The extracted solution was slowly added to the homogeneous solution with magnetic stirring. After stirring for 1 h, 2 mol L^{-1} of HNO₃ was added to adjust pH value of 7 and continuously stirred for 2 h, which was marked as solution A. A certain amount of AgNO₃ was dispersed in 20 mL of deionized water and marked as solution B. The solution B was slowly dropped into solution A, and the obtained yellow slurry was stirred continuously for 1 h at room temperature. Subsequently, the final mixture was transferred to a Teflon-lined stainless steel autoclave (100 mL) and aged at 110 °C for 12 h. After crystallization, the resulting gel was filtered, washed repeatedly with deionized water to pH value of 7 and dried at 80 °C. The as-synthesized product was calcined in air at 400 °C for 5 h to remove the template and form Ag NPs by the reduction of AgBr.

The desired level of Ag-AgBr in the catalyst was adjusted through varying the amount of AgNO₃. Bromide ion from CTAB was present in excess amounts to effectively precipitate AgBr. A train of Ag-AgBr/Al-MCM-41 was prepared with different Ag-AgBr content of 10, 30, 50, 70 and 90% and labeled as wt% Ag-AgBr/Al-MCM-41, respectively.

2.3. Fabrication of Ag-AgBr, Ag-AgBr/Pal and Ag-AgBr/MCM-41

To study the influences of different carriers and preparation methods on the activities of adsorption-photocatalysis, Ag-AgBr was prepared by the above-mentioned method without Al-MCM-41. Ag-AgBr/Pal and Ag-AgBr/MCM-41 were also synthesized via an impregnation–precipitation method. Briefly, acidified Pal and commercial MCM-41 supported a certain amount of AgNO₃, respectively, which were precipitated using excessive CTAB. Then, they were filtrated, dried at 80 °C and calcined at 400 °C for 5 h, respectively. The samples were prepared at a mass ratio of 1:1 (Ag-AgBr:

Pal or MCM-41) and labeled as 50% Ag-AgBr/Pal or 50% Ag-AgBr/MCM-41.

2.4. Characterization

The crystalline phase structure of as-prepared materials was determined by a ARL X'TRA X-ray diffractometer using Cu Kα radiation (λ = 0.154 nm) in the 2theta range of 1–10° and 5–80°. The XRD tests were performed using a 1.0° divergence slit, a 1.0° scatter slit and a 0.15 mm receiving slit. The data were recorded with a step size of 0.02° and scan speed of 1°/min in a proportional detector. The BET surface area was obtained by N₂ adsorption in a constant volume adsorption apparatus (Beekman Coulter SA 3100). The samples had been degassed at 200 °C for 2 h prior to measurement. Scanning electron micrographs (SEM) were recorded on a Zeiss Supra55VP SEM microscope at 5 kV. The transmission electron microscopy (TEM) analysis was performed on a JEM-2100 microscope, operating at 200 kV. The surface electronic state was identified through X-ray photo-electron spectroscopy (XPS) performed on a PHI 5000 Versa Probe electron spectrometer using Al Kα radiation. The scans with 10 sweeps were obtained with passing energy of 100 eV and a step size of 1 eV. For the high resolution scans, 20 sweeps were used with passing energy of 20 eV and a step size of 0.1 eV. The UV–vis diffuse reflectance spectra (DRS) were analyzed by a Shimadzu UV2550 spectrophotometer with BaSO₄-coated integrating sphere in the wavelength range of 300–800 nm. The photoluminescence (PL) spectra were collected by a HORIBA Fluoromax-4 with an excitation wavelength at 400 nm. The Ag content of samples was analyzed by ICP (Vista-AX). Photocurrent analyses were conducted on an electrochemical analyzer (CHI660B Instrument) in a standard three-electrode system. A platinum wire and a saturated calomel electrode were used as counter electrode and reference electrode, respectively. Working electrode was prepared as follows: 0.5 mL of sample slurry (0.2 g mL^{-1}) was drop-casted onto a piece of FTO slice with a fixed area of 1 cm², which was dried at 80 °C for 1 h. The electrolyte was an aqueous solution of 0.5 mol L^{-1} Na₂SO₄. A 500 W Xe lamp served as the light source. Electron paramagnetic resonance (EPR) spectra were recorded at room temperature on a Bruker model EPR JES-FA200 spectrometer using spin-trap reagent DMPO (Sigma Chemical Co.).

2.5. The tests of adsorption-photocatalysis and analytical methods

BF, CV and aniline were chosen as the target pollutants to probe the activities of adsorption-photocatalysis of as-prepared materials. In a typical test, 50 mg of a sample was dispersed in 100 mL of 50 mg L^{-1} BF (CV or aniline) aqueous solutions. Four groups of white LED lamp board (18 W/lamp board) were used as light source. Prior to the irradiation, this suspension was stirred in the dark for 30 min to achieve the adsorption/desorption equilibrium. After turning on the lamp, 5.0 mL of suspension was taken at certain time intervals (30 min) and centrifuged to remove the particles.

The analytical liquid was measured by a UV–vis spectrophotometer (EU-2600R Shanghai Onlab Instruments Co. Ltd., China). According to the respective characteristic absorption peak of BF at 543 nm (CV = 595 nm or aniline = 265 nm), the concentration of the sample was calculated with the standard work curve obtained previously. The removal rate R of BF (CV or aniline) was calculated by the Eq. (1).

$$R = \frac{C_o - C_t}{C_o} \times 100\% \qquad (1)$$

In which, C_o denoted the initial concentration of BF (CV or aniline), and C_t was the concentration at reaction time t.
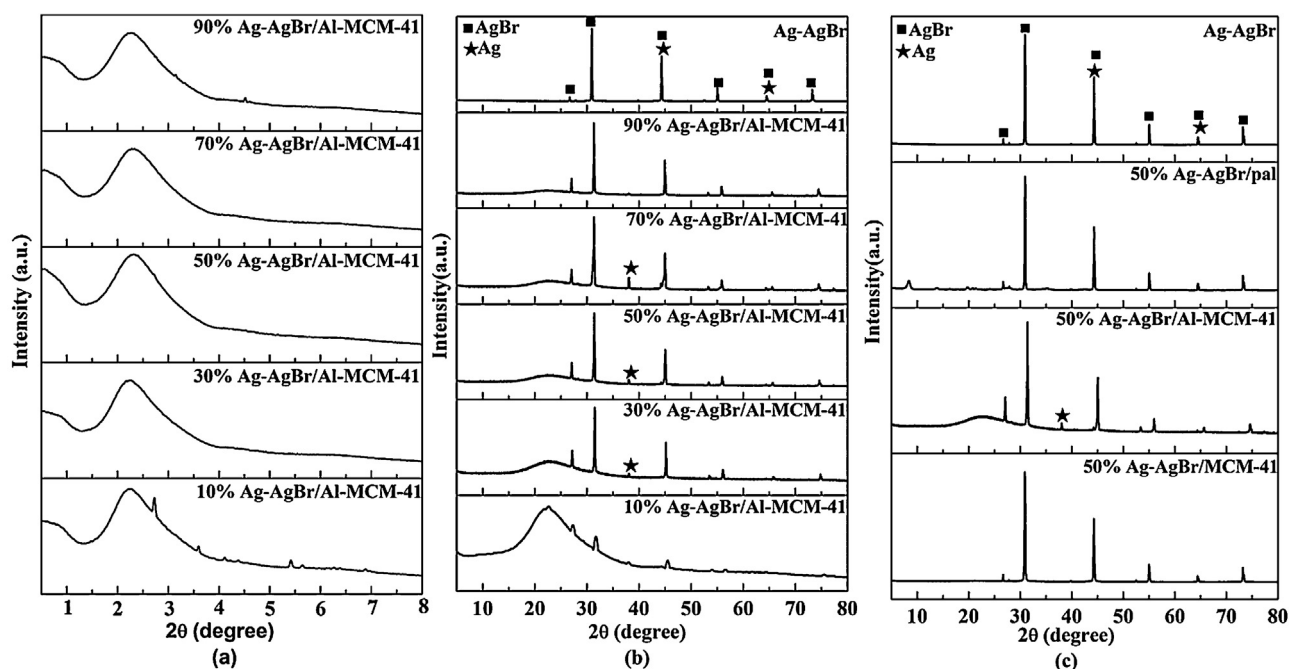
Fig. 1. XRD patterns of (a) 10–90% Ag-AgBr/Al-MCM-41 in the 2θ range of 0–8°, (b) Ag-AgBr and 10–90% Ag-AgBr/Al-MCM-41 in the 2θ range of 5–80°, (c) Ag-AgBr, 50% Ag-AgBr/Pal, 50% Ag-AgBr/Al-MCM-41 and 50% Ag-AgBr/MCM-41 in the 2θ range of 5–80°.

3. Results and discussion

3.1. Characterizations of as-prepared samples

Phase structure and crystallinity of as-fabricated samples are given in Fig. 1. All small-angle XRD patterns of 10–90% Ag-AgBr/Al-MCM-41 showed a reflection characteristic of the (1 0 0) crystal plane of Al-MCM-41 at 2θ = 2.43° (Fig. 1a), which was unchanged with increasing amount of Ag-AgBr [38]. This indicates that the deposition of Ag-AgBr on the Al-MCM-41 surface does not destroy well-fined ordered mesostructure of Al-MCM-41. As presented in Fig. 1b, the diffraction reflections at 26.7°, 31.0°, 44.3°, 55.0°, 64.5° and 73.4° were identified as the (1 1 1), (2 0 0), (2 2 0), (2 2 2), (4 0 0) and (4 2 0) planes of cubic AgBr (JCPDS 06-0438), respectively [27]. The reflections at 44.3° and 64.5° were assigned to the (2 0 0) and (2 2 0) planes of metallic Ag (JCPDS 04-0783) [39]. It can be seen that the intensity of these diffraction reflections were gradually strengthened with increasing content of Ag-AgBr. Besides, for 30–70% Ag-AgBr/Al-MCM-41 samples, the reflection at 38.1° was perfectly indexed to the (1 1 1) plane of face-centered cubic phase of Ag (JCPDS 04-0783) [40]. The results confirm the presence of metallic Ag and suggest the formation of Ag-AgBr/Al-MCM-41.

When equal amounts of Ag-AgBr were loaded on different carriers, the XRD patterns of 50% Ag-AgBr/Pal, 50% Ag-AgBr/Al-MCM-41 and 50% Ag-AgBr/MCM-41 were similar to those of Ag-AgBr, except for the presence of the reflection at 38.1° attributed to the (1 1 1) plane of Ag in 50% Ag-AgBr/Al-MCM-41 (Fig. 1c). It demonstrates that different support and synthesis method have an important influence on crystalline structure of Ag-AgBr/Pal, Ag-AgBr/Al-MCM-41 and Ag-AgBr/MCM-41.

SEM and appearance images of natural Pal, acidified Pal, Al-MCM-41 from acidified Pal, Ag-AgBr and 50% Ag-AgBr/Al-MCM-41 are displayed in Fig. 2. It is seen that natural Pal clay was light yellow powder, and contained bulk bundles and aggregations stacked up with many rods or fibers of about 0.5–5 μm in length (Fig. 2a). After acidification, the bundles of fibrous structures disappeared and numerous rods or fibers with shorter length were uniformly dispersed, resulting in pores or voids with different sizes. The acidified

Pal was acquired as grey white powder (Fig. 2b). The Al-MCM-41 from acidified Pal presented as white power, and consisted of evenly distributed lamellar or spherical particles with cross-linked network, indicating that the rearrangement of Pal occurred after hydrothermal treatment and calcination (Fig. 2c). The appearance of Ag-AgBr was green power and a large number of pebble-like Ag-AgBr particles were stacked together (Fig. 2d). As shown in Fig. 2e and f, the 50% Ag-AgBr/Al-MCM-41 was brown power. The active particles of Ag-AgBr were self-assembled on the surface and into mesoporous channel of Al-MCM-41. The obtained composite with a uniform coverage of Ag-AgBr particles remained good mesoporous structure.

Fig. 3 illustrates the TEM and HRTEM images of 50% Ag-AgBr/Al-MCM-41. It is clearly observed that some dark particles of Ag-AgBr with diameters in the range of 20–50 nm were evenly dispersed on the Al-MCM-41 (Fig. 3a and b). The HRTEM image of 50% Ag-AgBr/Al-MCM-41 is displayed in Fig. 3c, the lattice spacing of 3.89 nm corresponded to the (1 0 0) plane of Al-MCM-41, while the lattice spacing of 0.288 nm and 0.238 nm belonged to (2 0 0) plane of AgBr and (1 1 1) plane of Ag, respectively. The results of HRTEM further confirm that the particles of Ag-AgBr well anchor on the Al-MCM-41.

The nitrogen adsorption–desorption isotherms of 50% Ag-AgBr/pal, 50% Ag-AgBr/Al-MCM-41 and 50% Ag-AgBr/MCM-41 were categorized as type IV with hysteresis loop (Fig. 4), which is the characteristic of mesoporous material. Compared to 50% Ag-AgBr/pal and 50% Ag-AgBr/MCM-41, the adsorption amount of 50% Ag-AgBr/Al-MCM-41 increased more significantly at a relative low pressure ($P/P_0 < 0.4$), which is due to its larger specific surface area promoting monolayer adsorption of nitrogen towards the walls of the mesopores. Similarly, the adsorption amount of 50% Ag-AgBr/Al-MCM-41 increased drastically than those of 50% Ag-AgBr/pal and 50% Ag-AgBr/MCM-41 at the pressure range of 0.4–1.0. It implies that total mesopore volume of 50% Ag-AgBr/Al-MCM-41 is larger than those of 50% Ag-AgBr/pal and 50% Ag-AgBr/MCM-41, respectively. In addition, desorption curves of 50% Ag-AgBr/pal and 50% Ag-AgBr/Al-MCM-41 were narrower than that of 50% Ag-AgBr/MCM-41. It indicates that the mesopore size
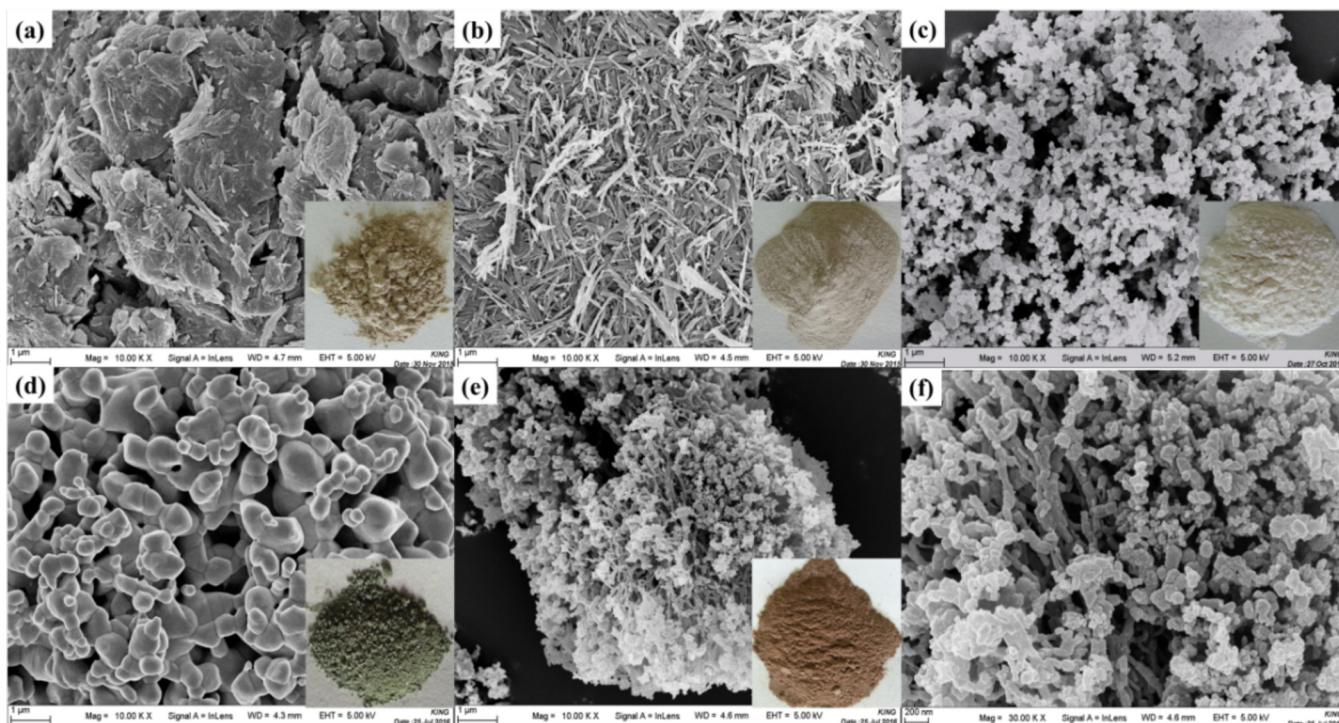
Fig. 2. SEM and appearance images of (a) natural Pal, (b) acidified Pal, (c) Al-MCM-41 from acidified Pal, (d) Ag–AgBr and (e, f) 50% Ag–AgBr/Al-MCM-41.
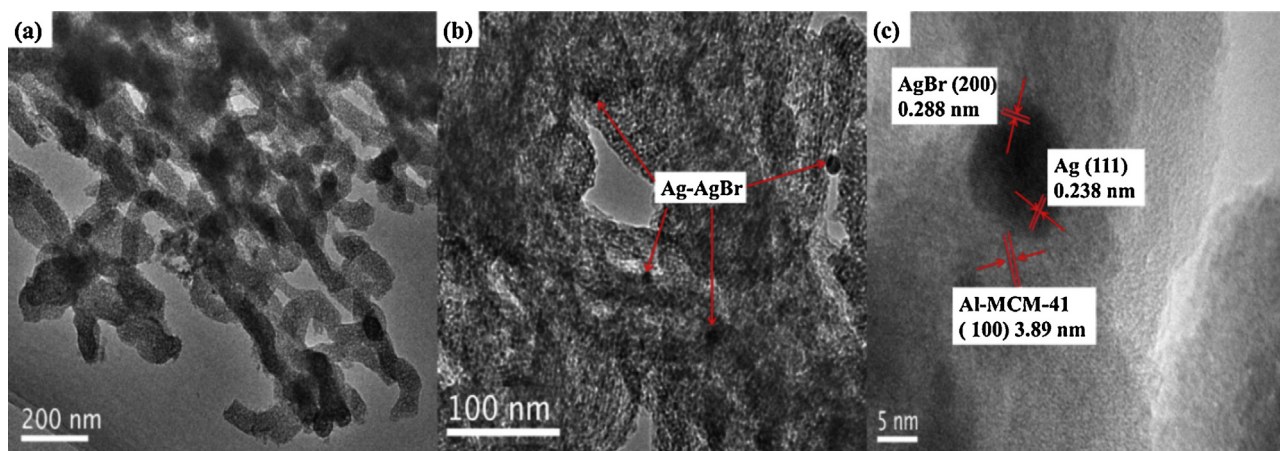

Fig. 3. TEM images (a, b) and HRTEM image (c) of 50% Ag-AgBr/Al-MCM-41.

of 50% Ag-AgBr/pal and 50% Ag-AgBr/Al-MCM-41 is more uniform than that of 50% Ag-AgBr/MCM-41. The specific surface area, pore volume and pore diameter of as-prepared samples are listed in Table S1.

The surface chemical composition and valence state of Ag-AgBr, 50% Ag-AgBr/Al-MCM-41 and Al-MCM-41 were analyzed by XPS. It can be found that the peaks appeared in the survey spectra are consistent with their elemental composition, except for the C 1s peak at 284.82 eV originating from adventitious hydrocarbon in the XPS instrument (Fig. 5a). The peaks of Ag 3d of Ag-AgBr and 50% Ag-AgBr/Al-MCM-41 are displayed in the high-resolution XPS spectra (Fig. 5b). For Ag-AgBr, two typical bands from Ag $3d_{5/2}$ and Ag $3d_{3/2}$ could be further divided into four different peaks. The peaks of Ag $3d_{5/2}$ at 366.92 and Ag $3d_{3/2}$ at 372.68 eV correspond to Ag$^+$, while the peaks of Ag $3d_{5/2}$ at 367.50 and Ag $3d_{3/2}$ 373.14 eV belong to Ag^0. Similarly, for 50% Ag-AgBr/Al-MCM-41, the peaks at 367.58 and

373.56 eV are attributed to Ag$^+$, and those at 368.28 and 374.20 eV belong to Ag^0 [41].

Fig. 5c shows the peaks of Br $3d_{5/2}$ and Br $3d_{3/2}$ with the binding energies of 68.35 and 69.27 eV for Ag-AgBr, 68.52 and 69.48 eV for 50% Ag-AgBr/Al-MCM-41, all of which are assigned to Br$^-$ [40]. Compared to the binding energies of Ag 3d and Br 3d of Ag-AgBr, those of Ag 3d and Br 3d of 50% Ag-AgBr/Al-MCM-41 had a shift to high energy. It might be due to the fact that the chemical bond of Ag-O-Ag between Ag-AgBr and Al-MCM-41 was formed. The XPS spectrum evidently proves the successful hybridization between Ag-AgBr and Al-MCM-41, and the existence of metal Ag^0, Ag$^+$ and Br$^-$ in the composite.

The UV–vis DRS in the wavelength range of 300–800 nm for 10–90% Ag-AgBr/Al-MCM-41, 50% Ag-AgBr/Pal, 50% Ag-AgBr/MCM-41 and Ag-AgBr are depicted in Fig. 6. It is observed that 10–90% Ag-AgBr/Al-MCM-41 exhibited superior capacity of light
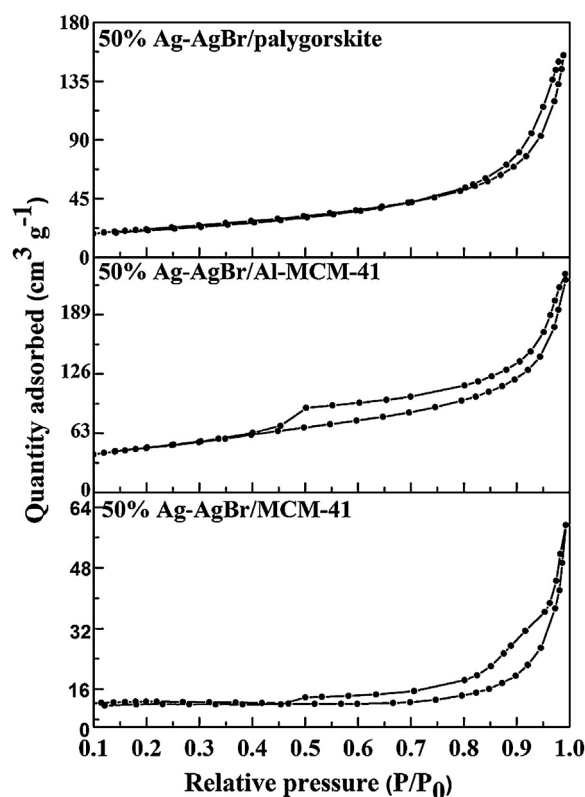
Fig. 4. Nitrogen adsorption–desorption isotherms of 50% Ag-AgBr/Pal, 50% Ag-AgBr/Al-MCM-41 and 50% Ag-AgBr/MCM-41.

absorption in a wide wavelength scope ranged from 400 to 800 nm. Among them, 50% Ag-AgBr/Al-MCM-41 possessed the strongest capability of light absorption (Fig. 6a). As shown in Fig. 6b, the photo-absorption edge of Ag-AgBr was about 510 nm due to its band gap of approximately 2.40 eV. The photo-absorption edges of 50% Ag-AgBr/MCM-41, 50% Ag-AgBr/Pal and 50% Ag-AgBr/Al-MCM-41 had a gradual shift to longer wavelength and displayed much stronger absorbance, which are attributed to the synergetic effect of Ag and AgBr with different contents and different supports in the composites (Table S2).

The band-gap energy of a photocatalyst can be calculated by the formula (2).

$$\alpha h\nu = \left(Ah\nu - E_g\right)^{\frac{n}{2}} \tag{2}$$

Where α, ν, E_g and A are the absorption coefficient, light frequency, band gap and constant, respectively. In addition, n depends on the characteristic of the transition in a semiconductor, including direct transition (n = 1) or indirect transition (n = 4). Previous reports indicate that Ag-AgBr is an indirect band-gap material. The band-gap energy can be estimated from a plot of $(\alpha h\nu)^{1/2}$ vs the photon energy ($h\nu$).

The x-axis intercept of the tangent of the plot approaches the band-gap energy of a sample (Fig. 6c). In this work, the band-gap values of 50% Ag-AgBr/Al-MCM-41, 50% Ag-AgBr/Pal, Ag-AgBr and 50% Ag-AgBr/MCM-41 samples were approximately 1.25, 1.28, 2.40 and 2.50 eV, respectively. The results are in accord with their capacities of light absorption.

PL measurements were applied to determine the recombination behavior of carriers of as-prepared samples, which are presented in Fig. 7a. Lower recombination of carriers implies higher separation efficiency of carriers. It is evident that Ag-AgBr displayed three strong PL signals locating at 480–500 nm and 520–560 nm, which are assigned to the recombination of carriers. When Ag-AgBr was

loaded on different carriers, the samples obviously exhibited lower intensity of emission spectrum, which imply a more efficient transfer and separation of carriers between Ag-AgBr and supporters. In particular, the emission peak of 50% Ag-AgBr/Al-MCM-41 was almost quenched. It suggests that the recombination of carriers is greatly suppressed in the system constructed by self-assembled method.

Photocurrent tests were performed to further explore the recombination behavior of carriers of as-fabricated samples. The higher photocurrent value indicates lower recombination of carriers. As shown in Fig. 7b, the photocurrent sequence was 50% Ag-AgBr/Al-MCM-41 > 50% Ag-AgBr/Pal > 50% Ag-AgBr/MCM-41 > Ag-AgBr. It confirms that the recombination of carriers of 50% Ag-AgBr/Al-MCM-41 is significantly inhibited.

3.2. Formation mechanism of Ag-AgBr/Al-MCM-41

The formation process of Ag-AgBr/Al-MCM-41 is displayed in Fig. 8. Natural Pal is a kind of di-octahedral clay mineral built by discontinuous Mg-O or Al-O octahedral layers, alternated with continuous Si-O tetrahedral ones. After the treatment of Pal with HCl, its internal Mg-O or Al-O octahedral sheets were gradually dissolved, resulting in appearance of amorphous SiO_2. Then the mixture of acidified Pal and NaOH was calcined under high temperature. The Pal calcined alkali was suspended in deionized water to obtain silicon aluminum source. At the same time, a certain amount of CTAB and $AgNO_3$ solutions were respectively added into the above suspension. Through the normal hydrothermal process, CTAB as a template interacted with silicon aluminum source to form rod-like micelles. In addition, it also provided bromide ion in excess amounts to produce AgBr with photocatalytic activity. By means of in situ synthesis, AgBr was installed uniformly into channels and surface of Al-MCM-41. Part of Ag was generated by the reduction of AgBr during the process of carbonization and removal of CTAB. Finally, Ag-AgBr/Al-MCM-41 was obtained with dual functions of adsorption-photocatalysis and SPR effect.

3.3. The performances of adsorption-photocatalysis of as-prepared samples

The performances of adsorption-photocatalysis of as-prepared samples were evaluated by comparing removal rates of BF, CV and aniline from water (Figs. 9–11). After adsorption for 30 min and light irradiation for 210 min, the 10% Ag-AgBr/Al-MCM-41 removed about 52% of BF, 65% of CV and 48% of aniline. The removal rates of BF, CV and aniline over 30% Ag-AgBr/Al-MCM-41 were approximately 72%, 92% and 52%. The 50% Ag-AgBr/Al-MCM-41 eliminated about 98% of BF, 99% of CV and 90% of aniline. Approximately 47% of BF, 38% of CV and 60% of aniline were expelled over 70% Ag-AgBr/Al-MCM-41. The removal rates of BF, CV and aniline over 90% Ag-AgBr/Al-MCM-41 were about 38%, 30% and 70%. The results indicate that the 50% Ag-AgBr/Al-MCM-41 possesses the strongest activities of adsorption-photocatalysis among 10–90% Ag-AgBr/Al-MCM-41.

To investigate effect of different carriers on activities of adsorption-photocatalysis of Ag-AgBr, the removal experiments of BF, CV and aniline were conducted over Ag-AgBr, 50% Ag-AgBr/Pal, 50% Ag-AgBr/MCM-41 and 50% Ag-AgBr/Al-MCM-41, respectively. The Ag-AgBr almost had no activities of adsorption-photocatalysis for the removal of BF and CV. The 50% Ag-AgBr/Pal eliminated approximately 10% of BF or CV via adsorption and about 15% adsorption removal of BF or CV was achieved over 50% Ag-AgBr/MCM-41. The 50% Ag-AgBr/Pal and 50% Ag-AgBr/MCM-41 showed no photocatalytic activities for the degradation of BF and CV. The removal rates of BF and CV over 50% Ag-AgBr/Al-MCM-41 were approximately 94% and 92% via adsorption, while about
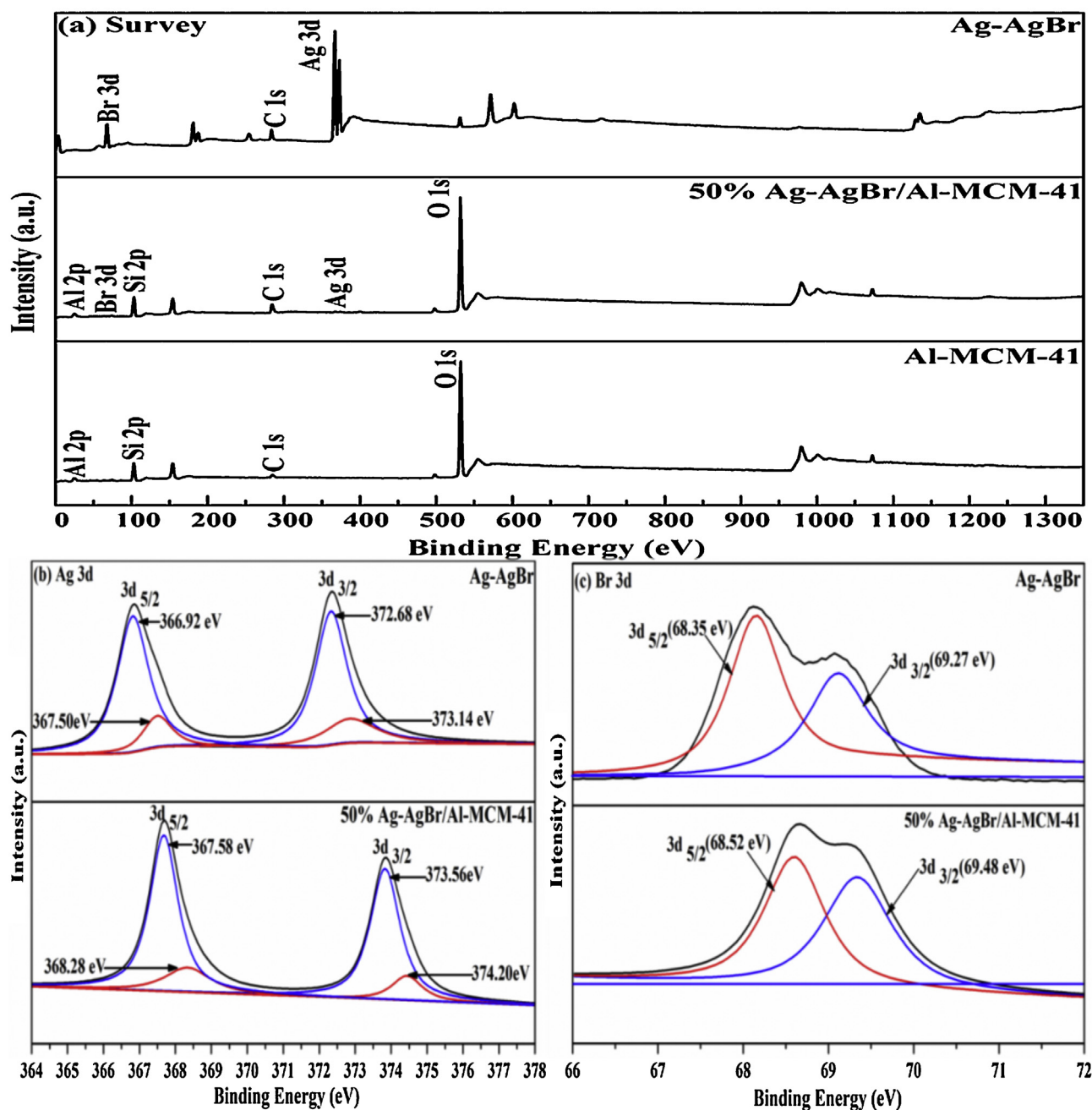
Fig. 5. XPS spectra of (a) Survey for Ag-AgBr, 50% Ag-AgBr/Al-MCM-41 and Al-MCM-41, (b) Ag 3d and (c) Br 3d for Ag-AgBr and 50% Ag-AgBr/Al-MCM-41.

4% of BF and 7% of CV were further degraded from water by photocatalytic reactions over 50% Ag-AgBr/MCM-41. The removal of aniline over Ag-AgBr, 50% Ag-AgBr/Pal, 50% Ag-AgBr/MCM-41 and 50% Ag-AgBr/Al-MCM-41 was approximately 45%, 40, 29% and 52% via adsorption. The photodegradation of aniline over Ag-AgBr, 50% Ag-AgBr/Pal, 50% Ag-AgBr/MCM-41 and 50% Ag-AgBr/Al-MCM-41 were about 14%, 30, 27 and 38%.

The stability of 50% Ag-AgBr/Al-MCM-41 is also a critical issue for long-term repeated use in practical application. The recycling experiments were further conducted to investigate its stability under the same conditions (Fig. S2). As seen, the removal rates of BF, CV and aniline over 50% Ag-AgBr/Al-MCM-41 still remained high after four cycles, which indicate that the bi-functional material can keep stable after repeated use.

3.4. Investigation on enhanced the activities of adsorption-photocatalysis of 50% Ag-AgBr/Al-MCM-41

Specific surface area of a material plays an important role on its adsorption capacity. In generally, a material with larger specific surface area can adsorb more contaminants. The sequence of specific surface area is 50% Ag-AgBr/Al-MCM–41 > 50% Ag-AgBr/Pal > 50% Ag-AgBr/MCM–41 > Ag-AgBr. Thus, 50% Ag-AgBr/Al-MCM-41 exhibits the strongest adsorption capacity among them.

The reasons of enhanced photocatalytic activity of 50% Ag-AgBr/Al-MCM-41 are summarized as follows. First, the 50% Ag-AgBr/Al-MCM-41 can adsorb more pollutants due to its excellent adsorption capacity, which favors photocatalytic degradation
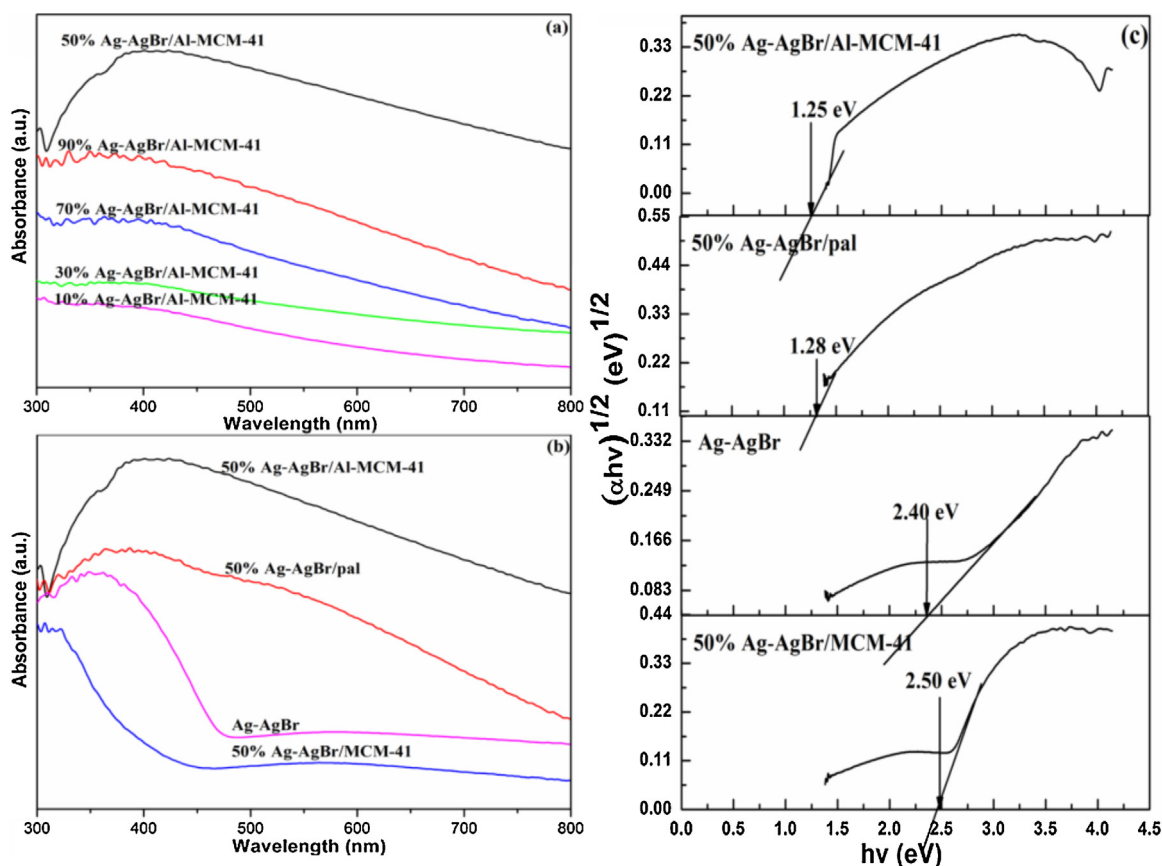
Fig. 6. (a) UV–vis diffuse reflectance spectra of 10–90% Ag-AgBr/Al-MCM-41, (b) UV–vis diffuse reflectance spectra and (c) the band-gap energies (E$_g$) of 50% Ag-AgBr/Al-MCM-41, 50% Ag-AgBr/Pal, Ag-AgBr and 50% Ag-AgBr/MCM-41.
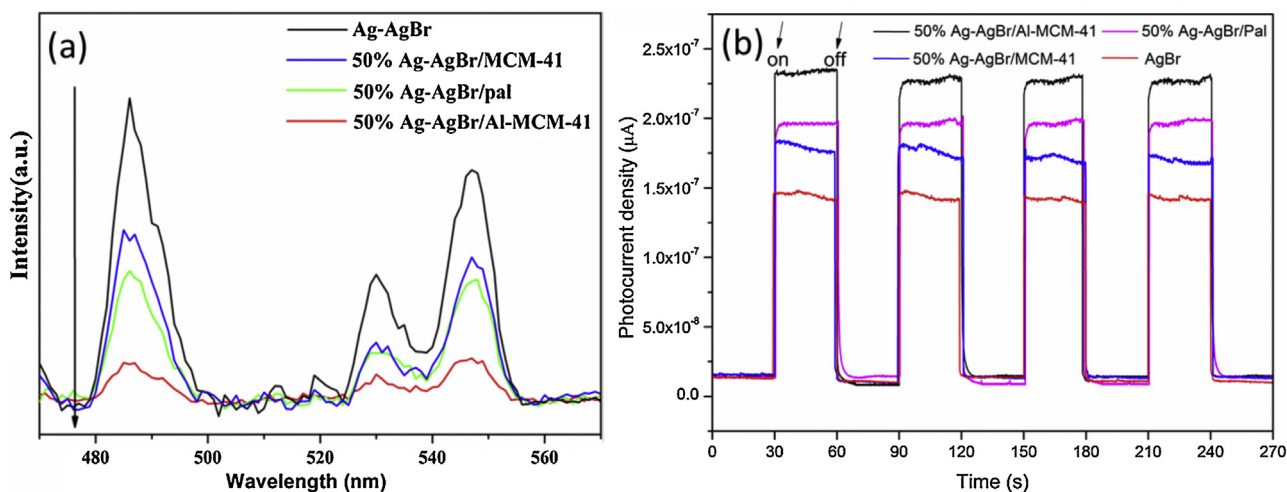

Fig. 7. (a) PL spectra and (b) photocurrent of Ag-AgBr, 50% Ag-AgBr/MCM-41, 50% Ag-AgBr/Pal and 50% Ag-AgBr/Al-MCM-41.

of the pollutants. Second, compared to 50% Ag-AgBr/Pal, 50% Ag-AgBr/MCM-41 and Ag-AgBr, a wider optical absorption range of 50% Ag-AgBr/Al-MCM-41 improves its photocatalytic activity. Finally, the efficient separation of photo-induced carriers of 50% Ag-AgBr/Al-MCM-41 boosts its photocatalytic activity.

3.5. Removal mechanisms of BF, CV and aniline

BF, CV and aniline over 50% Ag-AgBr/Al-MCM-41 were removed from water through dual roles of adsorption and photocatalysis (Fig. 12). First, the Al-MCM-41 adsorbs the contaminants on its surface. Then, they are further degraded by active species such as $^{\bullet}OH$ and h$^+$ under light irradiation. The reactive species originate mainly from AgBr and Ag. Under light irradiation, the electrons
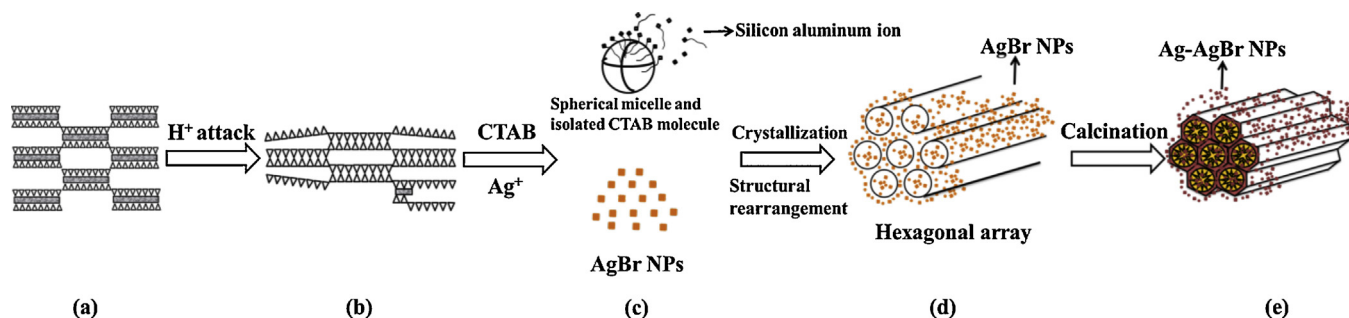
Fig. 8. Schematic illustration about synthesis of Ag-AgBr/Al-MCM-41 by self-assembly method: (a) natural Pal, (b) acidified Pal, (c) reactants for hydrothermal synthesis, (d) AgBr/Al-MCM-41 and (e) Ag-AgBr/Al-MCM-41.
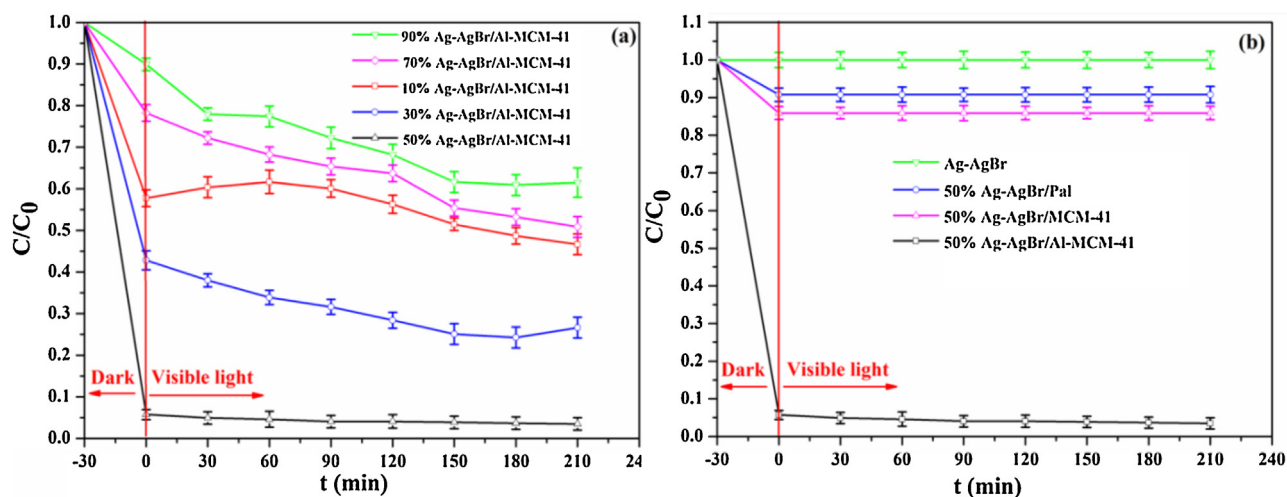

Fig. 9. Removal profiles of BF over (a) 10–90% Ag-AgBr/Al-MCM-41 and (b) Ag-AgBr, 50% Ag-AgBr/Pal, 50% Ag-AgBr/MCM-41 and 50% Ag-AgBr/Al-MCM-41.
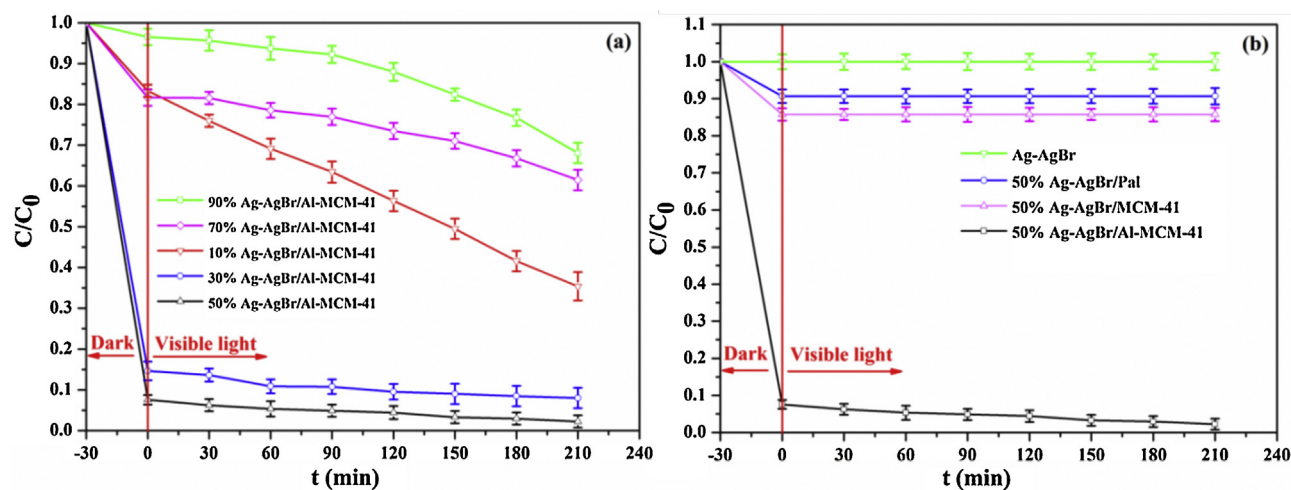

Fig. 10. Removal profiles of CV over (a) 10–90% Ag-AgBr/Al-MCM-41 and (b) Ag-AgBr, 50% Ag-AgBr/Pal, 50% Ag-AgBr/MCM-41 and 50% Ag-AgBr/Al-MCM-41.

of Ag SPR will inject to the conduction band of AgBr. The potential of conduction-band edge of AgBr is about 0.07 V [42], which is smaller than reduction potential of O_2/H_2O_2 ($E^o(O_2/H_2O_2) = 0.69$ V) [43]. Thence, the electrons from conduction-band edge of AgBr will react with O_2 and H^+ to form H_2O_2. Then, H_2O_2 with electrons is further decomposed into $^\bullet OH$. Almost no free radicals

of $^\bullet O_2^{-1}$ are generated during the photocatalytic degradation process. It is mainly due to the fact that reduction potential of O_2 ($E^0(O_2/^\bullet O_2^{-1}) = -0.33$ V/NHE) is smaller than potential of conduction-band edge of AgBr [43]. Therefore, photo-generated electrons can't react with O_2 to form $^\bullet O_2^{-1}$.
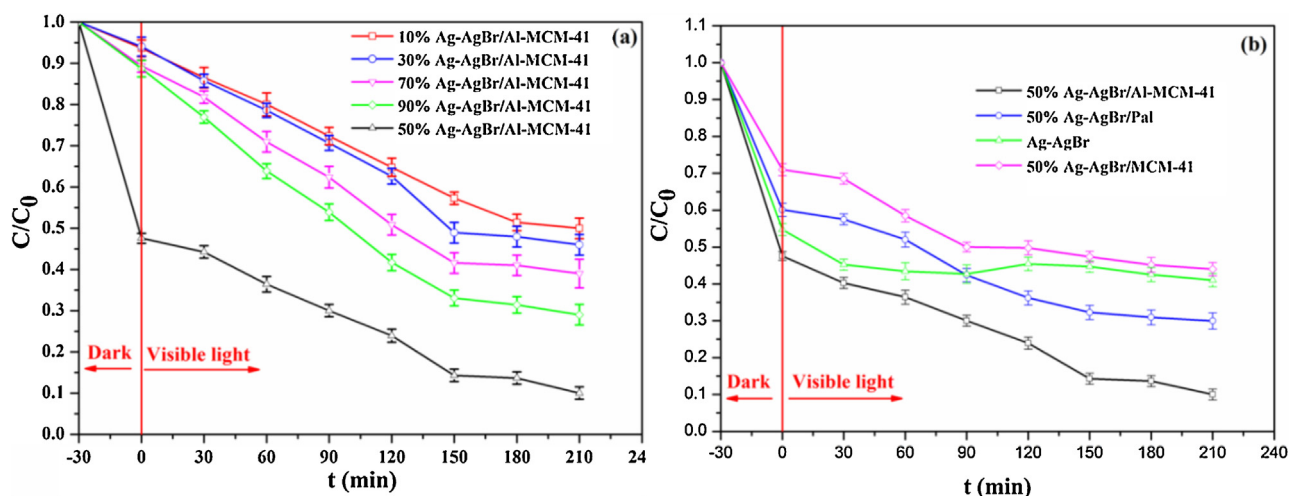
Fig. 11. Removal profiles of aniline over (a) 10–90% Ag-AgBr/Al-MCM-41 and (b) Ag-AgBr, 50% Ag-AgBr/Pal, 50% Ag-AgBr/MCM-41 and 50% Ag-AgBr/Al-MCM-41.
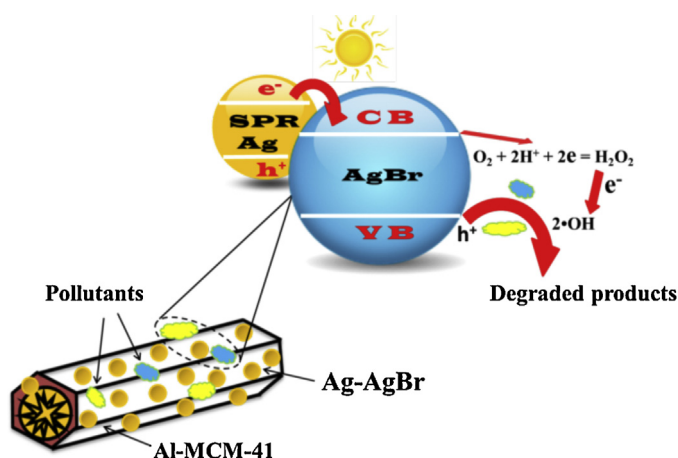

Fig. 12. Removal mechanisms of BF, CV and aniline over 50% Ag-AgBr/Al-MCM-41.

EPR spin-trap technique was conducted to determine $^\bullet$OH and $^\bullet O_2^{-1}$ radicals generated over 50% Ag-AgBr/Al-MCM-41 solution under light irradiation. As presented in Fig. 13, strong DMPO-$^\bullet$OH signals were clearly observed and $^\bullet O_2^{-1}$ signals were not found after light irradiation. In addition, a high photocurrent value verified the presence of photo-generated h$^+$ (Fig. 7b). Thus, the photocatalytic active species are $^\bullet$OH and h$^+$, which further confirm removal mechanisms of BF, CV and aniline.

4. Conclusions

In short, a bi-functional material of Ag-AgBr/Al-MCM-41 with excellent activities of adsorption-photocatalysis has been successfully fabricated. The optimal content of 50% Ag-AgBr loaded on the Al-MCM-41 exhibited the highest activity for the removal of BF, CV and aniline form water. It possessed good stability and reusability. This study signifies that the Ag-AgBr/Al-MCM-41 should be a promising material for the removal of toxic organic pollutants with high concentrations in wastewater.
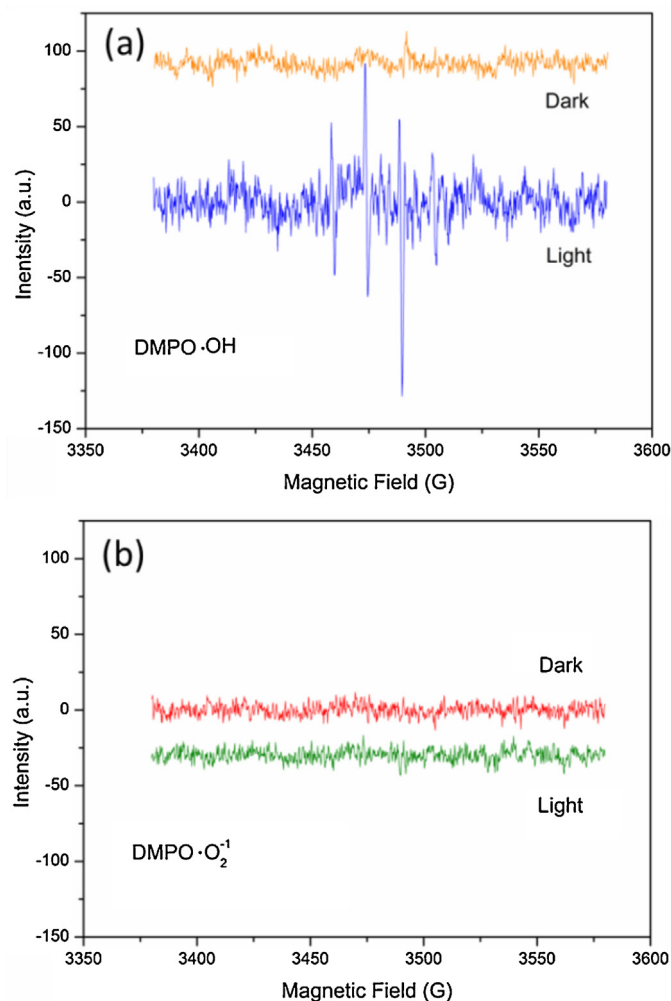

Fig. 13. EPR spectra for detecting (a) $^\bullet$OH and (b) $^\bullet O_2^{-1}$ of 50% Ag-AgBr/Al-MCM-41 solution using DMPO as a capture agent under light irradiation.

Appendix A. Supplementary data

Supplementary data associated with this article can be found, in the online version, at http://dx.doi.org/10.1016/j.apcatb.2017.01.082.

References

[1] N.A. Khan, Z. Hasan, S.H. Jhung, J. Hazard. Mater. 244 (2013) 444–456.
[2] X. Shen, L. Zhu, N. Wang, L. Ye, H. Tang, Chem. Commun. 48 (2012) 788–798.
[3] A.A.P. Mansur, H.S. Mansur, F.P. Ramanery, L.C. Oliveira, P.P. Souza, Appl. Catal. B-Environ. 158 (2014) 269–279.
[4] S.N. Garaje, S.K. Apte, S.D. Naik, J.D. Ambekar, R.S. Sonawane, M.V. Kulkarni, A. Vinu, B.B. Kale, Environ. Sci. Technol. 47 (2013) 6664–6672.
[5] P.S. Suchithra, C.P. Shadiya, A.P. Mohamed, P. Velusamy, S. Ananthakumar, Appl. Catal. B-Environ. 130 (2013) 44–53.
[6] W. Zhao, Y. Sun, F.N. Castellano, J. Am. Chem. Soc. 130 (2008) 12566–12567.
[7] J. Wang, P. Zhang, X. Li, J. Zhu, H. Li, Appl. Catal. B-Environ. 134 (2013) 198–204.
[8] S. Liu, J. Yu, M. Jaroniec, J. Am. Chem. Soc. 132 (2010) 11914–11916.
[9] J.W. Tang, Z.G. Zou, J.H. Ye, Angew. Chem. Int. Ed. 43 (2004) 4463–4466.
[10] M. Pelaez, N.T. Nolan, S.C. Pillai, M.K. Seery, P. Falaras, A.G. Kontos, P.S.M. Dunlop, J.W.J. Hamilton, J.A. Byrne, K. O'Shea, M.H. Entezari, D.D. Dionysiou, Appl. Catal. B-Environ. 125 (2012) 331–349.
[11] H. Wang, X. Yuan, Y. Wu, G. Zeng, X. Chen, L. Leng, H. Li, Appl. Catal. B-Environ. 174 (2015) 445–454.
[12] H. Wang, X. Yuan, Y. Wu, G. Zeng, H. Dong, X. Chen, L. Leng, Z. Wu, L. Peng, Appl. Catal. B-Environ. 186 (2016) 19–29.
[13] X. Yuan, H. Wang, Y. Wu, G. Zeng, X. Chen, L. Leng, Z. Wu, H. Li, Appl. Organomet. Chem. 30 (2016) 289–296.
[14] K. Mori, P. Verma, R. Hayashi, K. Fuku, H. Yamashita, Chem.-Eur. J. 21 (2015) 11885–11893.
[15] K. Fuku, R. Hayashi, S. Takakura, T. Kamegawa, K. Mori, H. Yamashita, Angew. Chem. Int. Ed. 52 (2013) 7446–7450.
[16] P. Verma, Y. Kuwahara, K. Mori, H. Yamashita, J. Mater. Chem. A 4 (2016) 10142–10150.
[17] P. Verma, Y. Kuwahara, K. Mori, H. Yamashita, J. Mater. Chem. A 3 (2015) 18889–18897.
[18] X.J. Bai, R.L. Zong, C.X. Li, D. Liu, Y.F. Liu, Y.F. Zhu, Appl. Catal. B-Environ. 147 (2014) 82–91.
[19] H. Zhang, H. Huang, H. Ming, H. Li, L. Zhang, Y. Liu, Z. Kang, J. Mater. Chem. 22 (2012) 10501–10506.
[20] X. Zhou, G. Liu, J. Yu, W. Fan, J. Mater. Chem. 22 (2012) 21337–21354.
[21] Z. Bian, T. Tachikawa, P. Zhang, M. Fujitsuka, T. Majima, J. Am. Chem. Soc. 136 (2014) 458–465.
[22] W.B. Hou, W.H. Hung, P. Pavaskar, A. Goeppert, M. Aykol, S.B. Cronin, ACS Catal. 1 (2011) 929–936.
[23] P. Wang, B. Huang, X. Qin, X. Zhang, Y. Dai, J. Wei, M.H. Whangbo, Angew. Chem. Int. Ed. 47 (2008) 7931–7933.
[24] C. An, S. Peng, Y. Sun, Adv. Mater. 22 (2010) 2570–2574.
[25] P. Wang, B.B. Huang, X.Y. Zhang, X.Y. Qin, Y. Dai, Z.Y. Wang, Z.Z. Lou, ChemCatChem 3 (2011) 360–364.
[26] P. Wang, B. Huang, X. Zhang, X. Qin, H. Jin, Y. Dai, Z. Wang, J. Wei, J. Zhan, S. Wang, J. Wang, M.H. Whangbo, Chem.-Eur. J. 15 (2009) 1821–1824.
[27] L. Kuai, B. Geng, X. Chen, Y. Zhao, Y. Luo, Langmuir 26 (2010) 18723–18727.
[28] J. Jiang, H. Li, L. Zhang, Chem.-Eur. J. 18 (2012) 6360–6369.
[29] Z. Wang, J. Liu, W. Chen, Dalton Trans. 41 (2012) 4866–4870.
[30] X. Xiao, L. Ge, C. Han, Y. Li, Z. Zhao, Y. Xin, S. Fang, L. Wu, P. Qiu, Appl. Catal. B-Environ. 163 (2015) 564–572.
[31] Z. Zheng, C. Chen, A. Bo, F.S. Zavahir, E.R. Waclawik, J. Zhao, D. Yang, H. Zhu, ChemCatChem 6 (2014) 1210–1214.
[32] C. Hu, T. Peng, X. Hu, Y. Nie, X. Zhou, J. Qu, H. He, J. Am. Chem. Soc. 132 (2010) 857–862.
[33] J.G. McEvoy, Z.S. Zhang, J. Photochem. Photobiol. A-Chem. 321 (2016) 161–170.
[34] M. Zhu, P. Chen, M. Liu, Langmuir 28 (2012) 3385–3390.
[35] Y. Xu, H. Xu, J. Yan, H. Li, L. Huang, Q. Zhang, C. Huang, H. Wan, Phys. Chem. Chem. Phys. 15 (2013) 5821–5830.
[36] Y. Yang, G. Zhang, Appl. Clay Sci. 67–68 (2012) 11–17.
[37] Y. Zhao, L. Kuai, B. Geng, Catal. Sci. Technol. 2 (2012) 1269–1274.
[38] N. Hao, F. Tang, L. Li, Microporous. Mesoporous Mater. 218 (2015) 223–227.
[39] A. Esmaeili, M.H. Entezari, J. Colloid Interface Sci. 466 (2016) 227–237.
[40] Y. Sui, C. Su, X. Yang, J. Hu, X. Lin, J. Mol. Catal. A-Chem. 410 (2015) 226–234.
[41] C. An, J. Wang, W. Jiang, M. Zhang, X. Ming, S. Wang, Q. Zhang, Nanoscale 4 (2012) 5646–5650.
[42] S. Wang, D. Li, C. Sun, S. Yang, Y. Guan, H. He, J. Mol. Catal. A-Chem. 383 (2014) 128–136.
[43] J. Kim, C.W. Lee, W. Choi, Environ. Sci. Technol. 44 (2010) 6849–6854.